Available online at www.sciencedirect.com
ScienceDirect
Journal of Sound and Vibration 309 (2008) 756–777
JOURNAL OF SOUND AND VIBRATION
www.elsevier.com/locate/jsvi

Nonlinear dynamics of a rub-impact micro-rotor system with scale-dependent friction model

Wen-Ming Zhang[a,*], Guang Meng[a], Di Chen[b], Jian-Bin Zhou[a], Jie-Yu Chen[a]

[a]*State Key Laboratory of Mechanical System and Vibration, Shanghai Jiao Tong University, Shanghai 200240, China*
[b]*National Key Laboratory of Micro/Nano Fabrication Technology, Key Laboratory for Thin Films and Microtechnology of Ministry of Education, Shanghai Jiao Tong University, Shanghai 200030, China*

Received 28 June 2006; received in revised form 18 May 2007; accepted 28 July 2007
Available online 27 September 2007

Abstract

Scale effects in dry friction at microscale and the coefficients of friction due to adhesion force and two- and three-body deformations are considered. A rub-impact micro-rotor model with scaling nonlinear rub-impact force is presented and the nonlinear dynamic characteristics of the system in micro-electro-mechanical systems (MEMS) are investigated when the rotating speed, imbalance, damping coefficient, scale length and fractal dimension are regarded as the control parameters. Effects of scale length, fractal dimension, velocity-dependent impact factor and contact form on the coefficients of dry friction are investigated and discussed, and used to study the nonlinear behavior of rub-related vibrations with a large number of numerical simulations. The effects of rotating speed, imbalance, damping coefficient, and friction coefficient on the micro-rotor system responses are studied. It is indicated that the rub-impact micro-rotor system with the scale effects in friction alternates among the periodic, quasi-periodic and chaotic motions as the system parameters change. The results can be effectively used to diagnose the rub-impact fault, reduce the failure and improve the characteristics of a micro-rotor system, and optimize the design of micro-rotating machinery in MEMS.

1. Introduction

Since the possible designs for electrostatic micromotors using technology derived from IC manufacturing processes was first discussed by Trimmer and Gabriel [1] in 1987 and the term "Power MEMS" was first suggested by Epstein et al. [2] in 1996 to describe microsystems which generated power or pumped heat, many micro-rotating machinery have been developed using silicon micromachining and other micro-electro-mechanical systems (MEMS) fabrications, including electrostatic micromotor, electromagnetic micromotor, micro-gas turbine engine, micro-rocket engine, micro-compressor and MEMS-based turbocharger, etc.

Micro-rotating machinery will be used in our future society for a wide range of energy conversion applications, electric power, mechanical power, fluid pumping, propulsion, ventilation and cooling included. However, there are many dynamic phenomena and nonlinear problems that can be met for micro-rotating

*Corresponding author. Tel.: +86 21 3420 6813.
E-mail address: wenmingz@sjtu.edu.cn (W.-M. Zhang).

0022-460X/$ - see front matter © 2007 Elsevier Ltd. All rights reserved.
doi:10.1016/j.jsv.2007.07.077

machinery in MEMS. At the rotating speed of more than a million rev/min to achieve efficiency targets, the "dry rubbing" phenomenon would lead to an unacceptably high drag and short service life [3]. Moreover, for micro-fabricated rotors, such balancing techniques have not yet been studied and developed [4]. Rotor imbalances are mainly contributed to the misalignment of the journal bearing and the DRIE etch non-uniformity [4,5]. It is expected that the imbalance is sufficient to force the rotor into solid contact with the stator when the maximum peak response near the natural frequency increases with the imbalance [4,5]. Rotor imbalance precludes performance of high-speed rotating machinery, promotes instability, reduces the range of stable operation, and then limits the maximum operational speed [5]. The clearance between the rotor and the bearing pin is so small that the rotor is intended to contact with the bearing pin when the motor is operating [6]. If the peak excursion exceeds the bearing clearance, the rotor would contact the wall [7].

Contact and friction affect the operation of many rotating machinery in MEMS, as well as the basic activities in nature. Many researches on analyzing [4,6,7] and simulating [8] the rotor dynamics in micro-rotating machinery have been done during the past two decades. The first experimental prediction of dynamic friction comes from the work on micromotor dynamics by Tai and Muller [9]. Beerschwinger et al. [10] successfully applied finite element analysis (FEA) to simulate a variable capacitance (VC) electrostatic micromotor, and calculated out the coefficient of friction. Epstein [7] gave two rotor dynamic design considerations, i.e. traversing the critical frequency and ensuring that the frequency for the onset of instability is above the operating range. In our previous works [11–14], contact characteristics, friction and wear of the rotor and bearing hub of micromotors have been studied, a linear sliding wear model with ratcheting effects has proposed to describe the wearing process and a simplified mathematical method has presented to simulate the wear and friction of the rotor bushing sliding on the ground plane in micromotors, and the reliability of the electrostatic micromotors has been reviewed and discussed. It can be concluded that the micro-rotor dynamics are underdamped but insufficient to develop a detailed model for the full dynamic behavior.

Rub-impact phenomenon is one of the malfunctions occurring often in rotating machinery and a rotor system with a fault is generally a complex nonlinear vibration system. However, conventional friction models lack characteristic length parameters, which would be responsible for scale effects. Researchers have recently investigated the scale effects in friction [15–19]. Hurtado and Kim [15] presented a micromechanical dislocation model (HK) of frictional slip between two asperities involved numerous parameters for single asperity contacts, but they did not propose a simple scaling law. Adams et al. [16] further extended their model for the behavior of the friction stress over a wide range of contact areas, including nanoscale and microscale contacts. They developed a multi-asperity model for contact and friction by incorporating the adhesion contact model of Maugis and the scale-dependent HK friction model into a statistical model with a Gaussian distribution of asperity summits. Furthermore, Adams and Muftu [20] presented a new scale-dependent contact and friction model to investigate three effects of Weibull distribution, non-constant radii of curvature of the asperity and non-contact asperities on contact and friction. The results showed that positive/negative skew decreases/increases the coefficient of friction and the coefficient of friction increases/decreases for radii of curvature that increase/decrease with height. Bhushan and Nosonovsky [17–19] presented a model for adhesional friction based on strain-gradient plasticity and dislocation-assisted sliding, developed a comprehensive model considered the scale effects on two- and three-body components of friction, and incorporated an empirical rule for the scale dependence of surface roughness parameters and a fractal description of the rough surface topography. A comprehensive friction model were developed by Tambe and Bhushan [21] to explain the velocity dependence of nanoscale friction over a wide range of velocities between $1\,\mu m\,s^{-1}$and $10\,mm\,s^{-1}$ on large scan lengths of 2 and 25 μm, considering the contributions of adhesion at the tip–sample interface, high impact velocity-related deformation at the contact asperities and atomic scale stick–slip.

A comprehensive investigation on the dynamic characteristics is of great importance to establish a reliable diagnosis system for micro-rotating machinery in MEMS. Due to needs for high speed and high efficiency in micro-rotating machinery, the clearance between the rotor and stator becomes smaller and smaller. There always exists the rotor imbalance contributed to the misalignment of the journal bearing and the DRIE etch non-uniformity. As a result, the rubbing phenomenon is one of the main problems in micro-rotating machinery. To make a profound understanding of the dynamic characteristics and malfunction faults of the micro-rotor system in MEMS, this study extends our previous work [22] and presents a general model of a

rub-impact micro-rotor system with the scaling effects in friction and analyzes its nonlinear dynamic characteristics using modern nonlinear dynamics and rotor dynamics theories. The phenomena and dynamic behavior, combining with other features such as bifurcation diagram, Poincaré maps, axes contrails, phase plane portraits and time histories, can make diagnosis much simpler within these limited types.

2. Mathematical model

2.1. Scale-dependent friction model

Friction force (F) is a tangential force resisting the relative motion of two surfaces, which are pressed against each other with a normal force (P). The dry friction between two bodies developed by Amontons and Coulomb can be expressed by defining the coefficient of friction μ as

$$\mu = \frac{F}{P}. \tag{1}$$

From the adhesion and deformation model of friction, the total friction force equals to the force needed to shear adhered junctions and the force needed to supply the energy of deformation, and the coefficient of dry friction μ can be given by a sum of the adhesion component μ_a and the deformation component μ_d [17,23]. The deformation component includes the asperity summit deformation component μ_{ds} and the particle deformation component μ_{dp} due to the wear particles. Therefore, the total coefficient of friction can be written as

$$\mu = \mu_a + \mu_{\mathrm{ds}} + \mu_{\mathrm{dp}}. \tag{2}$$

All real surfaces are rough and the contact and friction between two surfaces is carried by the asperities on the surfaces. For two rough surfaces in contact, the contact can be simplified by considering a rough surface with composite roughness parameters in contact with a smooth surface [24]. However, models to predict the friction force in a multi-asperity contact are relatively few. The classical microcontact GW model and more comprehensive models had been used to study the contact and friction between a single rough surface and a smooth one [24]. When multiple-asperity comes into contact, the scale dependence of surface roughness is a factor contributed to the scale dependence of the real area of contact [17].

Surface roughness parameters include the distribution of asperity heights, material properties, contact load, real contact area and the number of contact asperities [24]. Surface roughness has an appreciable influence on adhesive friction. Majumdar and Bhushan [25] developed a fractal model for modeling roughness with multiple length scales. The adhesional component of friction depends on the real area of contact and adhesion shear strength. In the case of predominantly elastic contact, the adhesional component of the coefficient of friction μ_a, for the fractal model [17,18], can be given by

$$\mu_a = \mu_{a0} \frac{\sqrt{1 + (L_s/L)^{(1-D)/2}}}{\sqrt{1 + l_s/\bar{a}}} \left(\frac{L}{L_{|W|}}\right)^{(D-2)/2}, \tag{3}$$

where μ_{a0} is the coefficient of friction at macroscale ($L \geqslant L_{|W|}$), L is the scan length which equals to nominal contact length, $L_{|W|}$ is the long-wave length limit, l_s is a material-specific characteristic length parameter, L_s is a characteristic length parameter related to l_s, $\bar{a}$ is the mean contact radius, and D is a fractal dimension.

Bhushan [23] calculated ploughing component of the friction force for four models related to rigid asperities or trapped wear particles, i.e. conical, spherical, and cylindrical with two orientations. The two-body deformation component of the coefficient of friction at microscale can be given by

$$\mu_{\mathrm{ds}} = \begin{cases} \mu_{\mathrm{ds0}} \left(\dfrac{L}{L_{|W|}}\right)^{1-D} & \text{conical shape,} \\ \mu_{\mathrm{ds0}} \left(\dfrac{L}{L_{|W|}}\right)^{(2-3D)/2} & \text{spherical shape,} \end{cases} \tag{4}$$

where μ_{ds0} is the two-body deformation component of the coefficient of friction at macroscale ($L \geqslant L_{|W|}$).

In the presence of three-body deformation, the probability for a particle of a given size to be trapped at the interface depends on the size of the region of contact [17,19]. Bhushan and Nosonovsky [19] considered a square region of contact of two rough surfaces with a length L and the density of debris of η particles per unit area. The three-body deformation component of the coefficient of friction can be obtained as

$$\mu_{\mathrm{dp}} = \mu_{\mathrm{dp0}} n_{\mathrm{tr}} \frac{\bar{d}^2}{\bar{d}_0^2} \frac{\sqrt{1+2l_d/\bar{d}}}{\sqrt{1+2l_d/\bar{d}_0}}, \tag{5}$$

where l_d is a material-specific characteristic length parameter, n_{tr} is the number of trapped particles divided by the total number of particles, $\bar{d}$ is the mean particle diameter, $\bar{d}_0$ is the macroscale value of the mean particle diameter, and the macroscale value of the three-body deformation component of the coefficient of friction μ_{dp0}, with $n_{\mathrm{tr}} = 1$ and $L \to \infty$, is given by

$$\mu_{\mathrm{dp0}} = \eta \frac{L^2}{P} \frac{\pi \bar{d}_0^2}{4} \tau_{Y0} \sqrt{1+2l_d/\bar{d}_0}, \tag{6}$$

where τ_{Y0} is the macroscale value of shear yield strength.

Introducing two scale parameters ψ_1 and ψ_2 and combining Eq. (2) with Eqs. (3)–(5), the expression for the total value of the coefficient of friction, for conical shape asperities, can be rewritten as

$$\mu = \mu_{a0} \left[\frac{\sqrt{1+(L_s/L)^{(2-D)/2}}}{\sqrt{1+l_s/\bar{a}}} \left(\frac{L}{L_{|W|}}\right)^{(D-2)/2} + \psi_1 \left(\frac{L}{L_{|W|}}\right)^{1-D} + \psi_2 \Psi \frac{\sqrt{1+2l_d/\bar{d}}}{\sqrt{1+(L_s/L)^{(2-D)/2}}} \right], \tag{7}$$

where $\psi_1 = \mu_{\mathrm{ds0}}/\mu_{a0}$, $\psi_2 = \mu_{\mathrm{dp0}}/\mu_{a0}$, and Ψ is a scale dependence parameter and can be given by

$$\Psi = \Psi_0 \frac{\sqrt{1+l_s/\bar{a}}}{\sqrt{1+(L_s/L)^{(2-D)/2}}} \left(\frac{L}{L_{|W|}}\right)^{(D-2)/2}, \tag{8}$$

where Ψ_0 is the macroscale value of transition index.

2.2. Rub-impact forces

It is assumed that the heating effects due to friction can be ignored. Compared with one complete period of rotating, the time during rub-impact is so short that the contact between the stator and rotor in the micro-rotor system can be regarded as elastic impact. Under these assumptions, the rub-impact micro-rotor model is illustrated in Fig. 1. As shown in Fig. 1, F_n is the radial impact force, F_τ is the tangential rub force, ϕ is the inclination angle between the direction radius of the contact point and X-axis and ω is the angular rotating speed of the micro-rotor.

Many materials are known to show a dependence of the sliding velocity on the coefficient of friction. In general, the coefficient of a monotonic sliding friction can be described by relative velocity V_{rel} and three independent friction parameters [26], i.e.

$$\mu(V_{\mathrm{rel}}; \mu_0, \mu_1, \alpha) = \mu_0 + \mu_1 \exp(-\alpha |V_{\mathrm{rel}}|), \tag{9}$$

where μ_0 governs the large relative velocity behavior, μ_1 controls the low velocity behavior, and α represents the impact factor due to the relative velocity.

The most prominent friction model in the system dynamics is often assumed to be monotonically weakening with increasing velocity and can be given by a simple velocity-dependent friction. For simplicity, the right-hand side of Eq. (9) can be linearized by Taylor series about the steady sliding equilibrium and can be simplified as

$$\mu_n = \mu + \alpha V_{\mathrm{rel}}^n, \tag{10}$$

where n is the index of the relative velocity-dependent term.

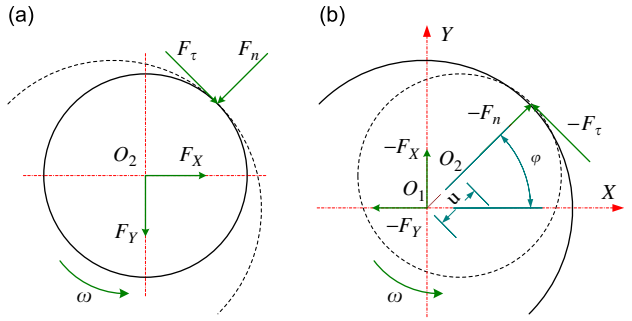

Fig. 1. Schematic diagram of the rub and impact forces between the rotor and stator.

Assuming that the radial deformation of the stator is linear and the friction relationship between the rotor and stator satisfies the above velocity-dependent friction laws with the scale effects. The rub and impact forces can then be given by

$$\begin{cases} F_n = k_r(u-\delta) \\ F_\tau = \mu_n F_n \end{cases} \quad (u>\delta), \qquad \begin{cases} F_n = 0 \\ F_\tau = 0 \end{cases} \quad (u\leqslant\delta), \tag{11}$$

where $u=\sqrt{X^2+Y^2}$ is the radial displacement of the rotor, k_r is the radial stiffness of the stator, and δ is an initial clearance between the rotor and the stator. The rub and impact forces can be written in $X-Y$ coordinates as

$$\begin{Bmatrix} F_X \\ F_Y \end{Bmatrix} = \begin{bmatrix} -\cos\varphi & \sin\varphi \\ -\sin\varphi & -\cos\varphi \end{bmatrix} \begin{Bmatrix} F_n \\ F_\tau \end{Bmatrix} = \begin{Bmatrix} 0 \\ 0 \end{Bmatrix} \quad (u\leqslant\delta) \tag{12a}$$

and

$$\begin{Bmatrix} F_X \\ F_Y \end{Bmatrix} = \begin{bmatrix} -\cos\varphi & \sin\varphi \\ -\sin\varphi & -\cos\varphi \end{bmatrix} \begin{Bmatrix} F_n \\ F_\tau \end{Bmatrix} = -\frac{k_r(u-\delta)}{u} \begin{bmatrix} 1 & -\mu_n \\ \mu_n & 1 \end{bmatrix} \begin{Bmatrix} X \\ Y \end{Bmatrix} \quad (u>\delta). \tag{12b}$$

2.3. The governing equations of motion

According to the rub and impact forces analyses and barycenter motion theorem, when the rotor rubs the stator, the Jeffcott micro-rotor system can be described by the following differential equation of motion:

$$\begin{bmatrix} m & \\ & m \end{bmatrix} \begin{Bmatrix} \ddot{X} \\ \ddot{Y} \end{Bmatrix} + \begin{bmatrix} c & \\ & c \end{bmatrix} \begin{Bmatrix} \dot{X} \\ \dot{Y} \end{Bmatrix} + \begin{bmatrix} k & \\ & k \end{bmatrix} \begin{Bmatrix} X \\ Y \end{Bmatrix} = \begin{Bmatrix} F_X \\ F_Y \end{Bmatrix} + me\omega^2 \begin{Bmatrix} \cos\omega t \\ \sin\omega t \end{Bmatrix}, \tag{13}$$

where $\dot{X}=\mathrm{d}X/\mathrm{d}t$ and $\dot{Y}=\mathrm{d}Y/\mathrm{d}t$, X and Y are the displacements of the axes centers of the micro-rotor in X and Y directions, respectively, m is the mass of the rotor, c is the damping coefficient, k is the stiffness coefficient and e is the imbalance.

The non-dimensional variables are defined as

$$\tau=\omega_0 t, \quad \Omega=\frac{\omega}{\omega_0}, \quad x=\frac{X}{\delta}, \quad y=\frac{Y}{\delta}, \quad \dot{x}=\frac{\mathrm{d}x}{\mathrm{d}\tau}, \quad \omega_0=\sqrt{\frac{k}{m}}, \quad \rho=\frac{e}{\delta}, \quad \upsilon=\frac{u}{\delta},$$
$$\xi=\frac{c}{2\sqrt{mk}}, \quad \beta=\frac{k_r}{k}. \tag{14}$$

Eq. (13) can be further rewritten in the following non-dimensional form:

$$\begin{cases} \ddot{x} + 2\xi\dot{x} + x + \beta(1 - \frac{1}{\upsilon})[x - \mu y - \alpha\omega_0\delta y(\dot{x}^2 + \dot{y}^2)^{n/2}] = \rho\Omega^2 \cos \Omega\tau \\ \ddot{y} + 2\xi\dot{y} + y + \beta(1 - \frac{1}{\upsilon})[\mu x + y + \alpha\omega_0\delta x(\dot{x}^2 + \dot{y}^2)^{n/2}] = \rho\Omega^2 \sin \Omega\tau \end{cases} \quad (\upsilon > 1). \tag{15}$$

Without rubbing against the stator, the governing equation of motion can be formulated as

$$\begin{cases} \ddot{x} + 2\xi\dot{x} + x = \rho\Omega^2 \cos \Omega\tau \\ \ddot{y} + 2\xi\dot{y} + y = \rho\Omega^2 \sin \Omega\tau \end{cases} \quad (\upsilon \leqslant 1). \tag{16}$$

3. Stability analysis

3.1. Stability of the solutions

During the process of micro-rotor is rotating at high speed, both Eqs. (15) and (16) have a steady-state periodic solution. For simplicity, setting $\alpha = 0$ and assuming that the solution has the following form:

$$\begin{cases} x = A \cos(\Omega\tau + \varphi), \\ y = A \sin(\Omega\tau + \varphi). \end{cases} \tag{17}$$

Due to the existence of the stator, the solution of Eq. (16) is eligible only when its amplitude A satisfies $A \leqslant 1$. The parameter equation in the parameter space where the solution exists can then be given by

$$(\rho^2 - 1)\Omega^4 + 2(1 - 2\xi^2)\Omega^2 - 1 \leqslant 0. \tag{18}$$

Provided that the other parameters are given, two real roots Ω_1 and $\Omega_2 (\Omega_1 < \Omega_2)$ can be derived by solving Eq. (18). The steady-state periodic solutions of the micro-rotor system (16) will exist only between Ω_1 and Ω_2 in the parameter regions.

For the governing equation of motion (15), the amplitude of its steady-state periodic solution can be obtained by substituting Eq. (17) into Eq. (15) and a polynomial of A can be given by

$$c_2 A^2 + c_1 A + c_0 = 0, \tag{19}$$

where

$$\begin{cases} c_2 = \Omega^4 + (4\xi^2 - 2 - 2\beta)\Omega^2 + 4\xi\beta\mu\Omega + (1 + 2\beta + \beta^2 + \beta^2\mu^2), \\ c_1 = 2\beta\Omega^2 - 4\xi\beta\mu\Omega + (-2\beta - 2\beta^2 - 2\beta^2\mu^2), \\ c_0 = -\rho^2\Omega^4 + \beta^2 + \beta^2\mu^2. \end{cases}$$

To get the boundary conditions where the solutions of Eq. (19) exist, Eq. (19) can be simplified with respect to A and the saddle-node bifurcation condition can be obtained

$$c_1^2 - 4c_0c_2 = 0. \tag{20}$$

From the physical viewpoint, A not only needs to be real and positive but also satisfies $A > 1$ to assure that contact occurs between the rotor and stator.

To analyze the stability of the micro-rotor system with rub-impact, it is necessary to review the eigenvalue issue of the governing equation of motion. Using the Laplace expansion formula, the associated characteristic equation can be given by

$$\lambda^4 + 4\xi\lambda^3 + (2 + 4\xi^2)\lambda^2 + 4\xi\lambda + 1 = 0. \tag{21}$$

According to the Routh–Hurwitz conditions, stability determinant condition of the steady-state periodic solution of Eq. (16) is

$$4\xi^2 + \xi > 0. \tag{22}$$

It is evident that condition (22) comes into existence at any condition ($\xi > 0$), i.e., the corresponding steady-state periodic solutions are stable. However, the rotor will rub with the stator due to the existence of the stator when the vibration amplitude is beyond the clearance.

When rub between the rotor and the stator happens, the motion of the micro-rotor system will then be governed by Eq. (15), and it is non-autonomous system and cannot be used to determine the stability of the system directly. Using the Laplace expansion formula of partitioned matrix, the associated characteristic equation can be given by

$$b_4\lambda^4 + b_3\lambda^3 + b_2\lambda^2 + b_1\lambda + b_0 = 0, \tag{23}$$

where

$$\begin{cases} b_4 = 1, \\ b_3 = 4\xi, \\ b_2 = 2\Omega^2 + 4\xi^2 - \frac{1}{A} + 4, \\ b_1 = 4\xi\Omega^2 + \left(4\mu - \frac{2}{A}\mu\right)\Omega + 8\xi - \frac{2}{A}\xi, \\ b_0 = \Omega^4 + \left(4\xi^2 + \frac{1}{A} - 4\right)\Omega^2 + \left(4\mu\xi - \frac{2}{A}\mu\xi\right)\Omega + \left(\mu^2 - \frac{2}{A}\mu^2 - \frac{2}{A} + 4\right) \end{cases}$$

and the values of these coefficients are functions of the amplitude A. From the viewpoint of the bifurcation theory, it is interested and significative to determine the bifurcation boundaries of the solutions.

The micro-rotor system with rub-impact has linear and cross stiffness, nonlinear rub and impact forces. If the partitioned matrix has one zero eigenvalue, the system will occur saddle-node bifurcation and the condition corresponds to $b_0 = 0$ in Eq. (23), i.e.

$$b_0 = \Omega^4 + \left(4\xi^2 + \frac{1}{A} - 4\right)\Omega^2 + \left(4\mu\xi - \frac{2}{A}\mu\xi\right)\Omega + \left(\mu^2 - \frac{2}{A}\mu^2 - \frac{2}{A} + 4\right) = 0. \tag{24}$$

For any amplitude A, the relationship between Ω and the other relative parameters can be obtained by combining Eqs. (19) and (24). We can then determine the condition in the parameter space where the saddle-node bifurcation of the steady-state periodic solutions of the micro-rotor system occurs.

From the Hopf bifurcation theorem, Hopf bifurcation of the solutions will appear if there is one pair of conjugate purely imaginary eigenvalues. Assuming the eigenvalues satisfy $\lambda = \pm\omega$ and substituting it into Eq. (23) yields

$$b_1^2 - b_1 b_2 b_3 + b_0 b_3^2 = 0. \tag{25}$$

Substituting $b_0 - b_3$ in Eq. (23) into Eq. (25) and combining Eqs. (19), (23) and (25), the polynomial of Ω, which can be used to determine the Hopf bifurcation condition of the nonlinear solutions at parameter space, can be obtained.

3.2. *Effects of system parameters on micro-rotor responses*

The effects of system parameters on rotor dynamical behavior as well as on rotor instability are investigated in this section. Among many effect factors, the effects of several main system parameters, rotating speed, imbalance, and damping and friction coefficients on micro-rotor responses in parameter place are analyzed and discussed.

Figs. 2–4 display the micro-rotor response characteristics on the parameter plane of different system parameter combinations among frequency ratio, imbalance, damping and friction coefficients. Fig. 2 shows the micro-rotor response characteristics on the parameter plane of the damping coefficient ζ and frequency ratio Ω for different imbalance. It is known from Eq. (22) that the linear periodic solution without rubbing of the micro-rotor system is always stable. However, since the existence of the clearance between the rotor and the stator, the solution cannot exist all over the parameter space. It can be seen from Eq. (18) that the amplitude of the steady-state periodic solution A satisfies $A \to 1$ at $\Omega = \Omega_1$ or Ω_2 when the forcing frequency approximates to the natural frequency of the micro-rotor, i.e., Ω approaches to 1, as illustrated in Fig. 2(a).

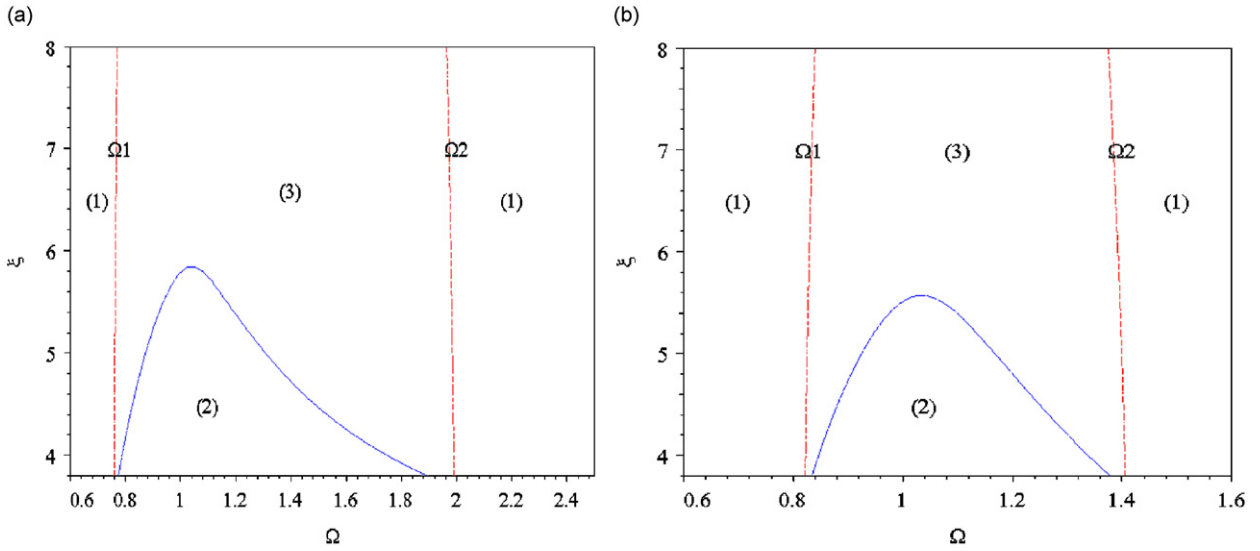

Fig. 2. Micro-rotor response characteristics on the parameter plane of the damping coefficient ζ and frequency ratio Ω for different imbalance: (a) $e = 3\,\mu m$ and (b) $e = 2\,\mu m$.

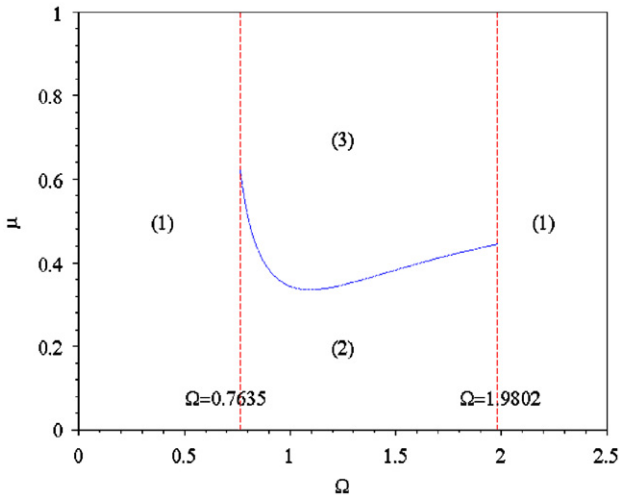

Fig. 3. Micro-rotor system responses on the parameter plane of the friction coefficient μ and frequency ratio Ω.

It is derived from Eqs. (20) and (24) that the rub solutions exist between Ω_1 and Ω_2. The result indicates that the region of rub solutions is determined by Ω_1 and Ω_2, and the disappearance of the rub solutions are not due to the bifurcation but due to the variation of the amplitude of the micro-rotor response. It can be observed from Fig. 2(a) that the periodic solutions of the micro-rotor system are stable in the region (1) and the dynamic behavior of the micro-rotor is a periodic no-rub motion. When Ω satisfies $\Omega_1 < \Omega < \Omega_2$, the periodic solutions of the micro-rotor system are unstable. From Hopf bifurcation condition (25), the Hopf bifurcation boundary can be determined, i.e., the boundary of the regions (2) and (3). The boundary is of a parabolic shape and has its highest point at $\Omega = 1$. Therefore, the unstable rub motions of the micro-rotor system can happen only in region (2). The steady-state periodic solutions in region (3) indicate that the rub motions of the micro-rotor system are stable and the stable motions like quasi-periodic ones. Moreover, the stability of the periodic solution becomes more and more evident with the increase of damping coefficient. After reducing the imbalance e (i.e., $e = 3\,\mu m \rightarrow e = 2\,\mu m$), the region of the rub motion (2) keeps down, the stable boundaries

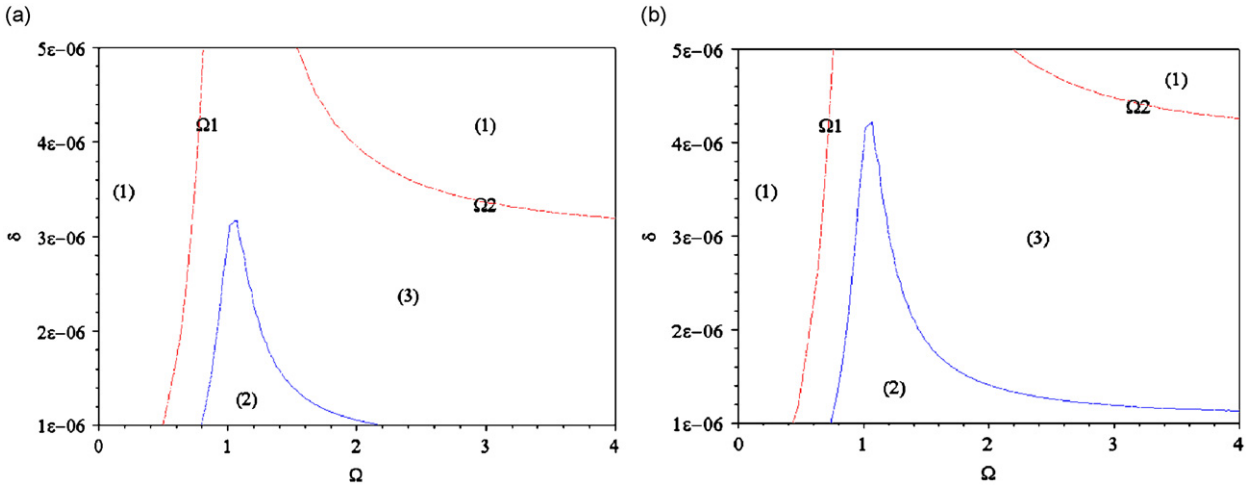

Fig. 4. Micro-rotor response characteristics on the parameter plane of the clearance between the rotor and stator δ and frequency ratio Ω for different imbalance: (a) $e = 3\,\mu m$ and (b) $e = 4\,\mu m$.

$\Omega = \Omega_1$ and Ω_2 close to middle direction, and the Hopf bifurcation boundary moves downwards, as displayed in Fig. 2(b). Therefore, the stable boundaries $\Omega = \Omega_1$ and Ω_2 vary correspondingly with the change of system parameters, and the rub motion will occur less with the decrease the imbalance.

As shown in Fig. 3, the periodic solutions of the micro-rotor system are stable in the parameter region (1) of $\Omega < \Omega_1 = 0.7635$ and $\Omega > \Omega_2 = 1.9802$ and the dynamic behavior of the micro-rotor is a periodic no-rub motion. When $\Omega_1 < \Omega < \Omega_2$, the rub motion of the micro-rotor system occurs and the steady-state periodic solutions of the micro-rotor system are unstable. From Hopf bifurcation condition (25), the Hopf bifurcation boundary can be obtained, namely, the boundary of the regions (2) and (3). The boundary is of a parabolic shape and has its lowest point at $\Omega = 1$. Therefore, the unstable rub motions occur in the region (3) and the rub solutions become more and more unstable for larger friction coefficients. The steady-state periodic solutions in region (2) indicate that the rub motions of the micro-rotor system are stable and the stable motions like quasi-periodic ones. When the friction coefficient increases, the unstable rub region of rub motions (3) extends and the rub motion will occur.

Fig. 4 displays the micro-rotor response characteristics on the parameter plane of the clearance between the rotor and stator δ and frequency ratio Ω. As shown in Fig. 4(a), at $\Omega = \Omega_2$, the rotor response produces the jump phenomena in the region (1) and the periodic solution of the rotor system is stable. When $\Omega_1 < \Omega < \Omega_2$, the periodic solution of the micro-rotor system is unstable. From Hopf bifurcation condition (25), the Hopf bifurcation boundary can be obtained, namely, the boundary of the regions (2) and (3). The boundary is of a parabolic shape and has its highest point at $\Omega = 1$. Therefore, the rub motion occurs in the region (2) and the steady-state periodic solutions are stable in the region (3), and this indicates that the rub motion is stable and the motion maybe becomes quasi-periodic motion. With the increase of imbalance e ($e = 3\,\mu m \rightarrow e = 4\,\mu m$), the region of the unstable rub motion (2) changes significantly, the stable boundary $\Omega = \Omega_2$ jumps evidently and expands outwards, and the Hopf bifurcation boundary moves upwards, as illustrated in Fig. 4(b). Therefore, the micro-rotor responses on the parameter plane will produce unstable rub motion in certain region around $\Omega = 1$ when the clearance δ is less than certain fixed value, meantime, the possibility of the unstable motion will reduce with the increase of δ. Moreover, as the increase of the imbalance, the stable boundaries $\Omega = \Omega_1$ and Ω_2 vary correspondingly with the change of system parameters and the boundary $\Omega = \Omega_2$ will jump when the imbalance becomes larger. It is indicated that the unstable rub motion will occur less with the decrease of imbalance.

Tables 1 and 2 list some parts of the eigenvalues of the micro-rotor system with different system parameter combinations. It can be seen from the results of these seven parameters combinations that the steady-state periodic solutions exist stable and unstable and the stability changes with the different parameter

Table 1
Different system parameter combinations and their descriptions

Parameter combination	System parameter description
1	$e = 3\,\mu m$, $f = 0.26$, $\Omega = 1.1$, $\delta = 4\,\mu m$
2	$e = 3\,\mu m$, $f = 0.26$, $\Omega = 2.1$, $\delta = 4\,\mu m$
3	$e = 3\,\mu m$, $f = 0.36$, $\Omega = 1.1$, $\delta = 4\,\mu m$
4	$e = 1\,\mu m$, $f = 0.36$, $\Omega = 1.1$, $\delta = 4\,\mu m$
5	$e = 3\,\mu m$, $f = 0.36$, $\Omega = 1.1$, $\delta = 2\,\mu m$
6	$e = 3\,\mu m$, $f = 0.36$, $\Omega = 3.1$, $\delta = 3\,\mu m$
7	$e = 3\,\mu m$, $f = 0.36$, $\Omega = 1.0$, $\delta = 3\,\mu m$

Table 2
Characteristics of the rub-impact micro-rotor system with different system parameter combinations

No.	Eigenvalue				Conclusion
	λ_1	λ_2	λ_3	λ_4	
1	−0.0192 + 2.4579i	−0.0192−2.4579i	−0.1808 + 0.2487i	−0.1808−0.2487i	Stable
2	−0.0488 + 3.3178i	−0.0488−3.3178i	−0.1512 + 0.8704i	−0.1512−0.8704i	Stable
3	0.0272 + 2.4655i	0.0272−2.4655i	−0.1986 + 0.2575i	−0.1986−0.2575i	Unstable
4	−0.0088 + 2.3491i	−0.0088−2.3491i	−0.3176	−0.0077	Stable
5	0.0345 + 2.4918i	0.0345−2.4918i	−0.2059 + 0.2900i	−0.2059−0.2900i	Unstable
6	−0.0061 + 4.3469i	−0.0061−4.3469i	−0.1653 + 1.8508i	−0.1653−1.8508i	Stable
7	0.0328 + 2.3859i	0.0328−2.3859i	−0.2043 + 0.3836i	−0.2043−0.3836i	Unstable

combinations. Since the results listed in Table 2 can be related to Figs. 2–4, it is easy to judge the stability of the steady-state periodic solutions and even the stability of the micro-rotor system and the stable region. For example, for the third pair of system parameter combination ($e = 3\,\mu m$, $f = 0.36$, $\Omega = 1.1$, $\delta = 4\,\mu m$), the real parts of the eigenvalues of the micro-rotor responses λ_1 and λ_2 are positive, this indicates that the periodic solution is unstable and the micro-rotor system can come into rubbing. It can be seen from the above qualitative analysis that the governing equation of motion has bifurcation for some system parameter combinations. Therefore, the micro-rotor system will become unstable for some system parameter combinations and may lead to chaos.

4. Results and discussions

4.1. Numerical simulations and results

Eq. (15) represents a nonlinear and non-autonomous system. When the rub-impact occurs, partial derivatives of the nonlinear terms F_X and F_Y do not exist due to the piecewise feature. However, the one-step method to numerically integrate the initial value problem of the ordinary differential equation is convergent when the Lipshitz condition is satisfied. Then the fourth-order Runge–Kutta method is used to integrate the set of Eqs. (15) and (16). A smaller integration step ($2\pi/200$) has to be chosen to ensure a stable solution and to avoid the numerical divergence at the point where derivatives of F_X and F_Y are discontinuous. Generally, long time-marching computation is needed to obtain a convergent orbit. For the sake of a strongly stable motion and eliminating the effect of free vibration, a few hundred periods of integration have to be neglected, while a few hundred periods of integration behind are retained.

To illustrate the dynamic behavior of the system, the bifurcation diagram, Poincaré maps, axes contrails, phase plane portraits, time histories and amplitude spectrum are used. The parameter values used in the calculation are as follows: the coefficient of dry friction due to elastic contact at macroscale $\mu_{a0} = 0.025$, index of the relative velocity-dependent term $n = 1$.

4.1.1. Effect of rotating speed

The rotating speed is one of the most important parameters affecting the dynamic characteristics of a micro-rotor system. Fig. 5 shows the bifurcation diagram of the micro-rotor system using the rotating speed as the control parameter with $\zeta = 0.025$ and $\rho = 0.5$. It can be seen that the rotor responses contains periodic and quasi-periodic motions alternately at the interval of $0 < \Omega < 5$. When $\Omega < 1.8$, the vibration amplitude of the micro-rotor is smaller, the rub phenomenon does not occur, the motion is synchronous with period-one (P-1), and only one point is correspondingly displayed in the bifurcation diagram for every rotating speed. With the increase of the rotating speed, rub does occur between the rotor and the stator. As $\Omega > 1.8$, the motion becomes quasi-periodic. Moreover, as the change of rotating speed continuously, the quasi-periodic motion becomes synchronous with P-1 again when $\Omega = 3.55$. Therefore, as the rotating speed increases, the changes of the system responses are very complex and mainly include periodic and quasi-periodic motions alternately.

When the scale effects in friction is considered, the bifurcation diagram of the micro-rotor system using the rotating speed as the control parameter is displayed in Fig. 6 with $\zeta = 0.025$, $\rho = 0.5$, $L_s/L_{|W|} = 1$, $L/L_{|W|} = 0.9$, $D = 1.9$, $\varphi_1 = 0.01$, $\varphi_2 = 0.1$ and $\alpha = 0.5$. It is obvious that the system response displays wider quasi-periodic motion when $\Omega > 0.3$. As the increase of the rotating speed, the system responses show synchronous motions with P-1 and quasi-periodic motion, quasi-periodic motion components increase with the scale effects in friction, and the quasi-periodic motions and synchronous periodic motions vary alternatively. In addition, the more greatly the rotating speed increases, the wider the range of quasi-periodic motion becomes and the larger the number of periodic motions appears.

To illustrate the various processes of motion, Figs. 7 and 8 show the nonlinear characteristics of the micro-rotor system with the plots of the Poincaré maps and axes contrails at different conditions. The motion of the micro-rotor system changes between P-1 and quasi-period alternately. The motion with P-1 represented by a point with the Poincaré maps becomes quasi-periodic motion characterized by a closed curve at $\Omega = 1.8$ and 3.55, as illustrated in Fig. 7. In Fig. 8, the synchronous motion with P-1 and quasi-periodic motion changes correspondingly for the same of Ω with the scale effect in friction. Moreover, the quasi-periodic motion components and synchronous motions with period-X become obvious. It is indicated that the motion of the micro-rotor displays periodic and quasi-periodic motions alternatively when the rotating speed is used as the control parameter with the scale effects in friction.

4.1.2. Effect of imbalance

For micro-rotating machinery in MEMS, there exists bigger imbalance due to the IC process and assembly. Imbalance is of great importance to the vibration of the micro-rotor system. During the operating process, a practical micro-rotating machinery imbalance will be changed unavoidably due to the effects from different

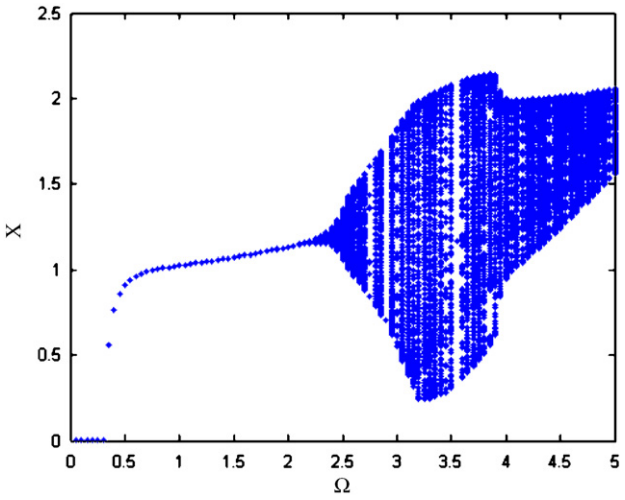

Fig. 5. The bifurcation diagram of Ω on the response of rubbing micro-rotor system with $\zeta = 0.025$ and $\rho = 0.5$.

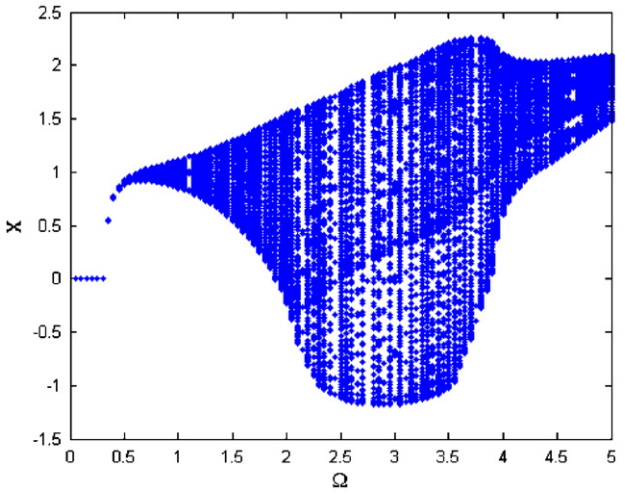

Fig. 6. The bifurcation diagram of Ω on the response of rubbing micro-rotor system with $\zeta = 0.025$, $\rho = 0.5$, $L_s/L_{|w|} = 1$, $L/L_{|w|} = 0.9$, $D = 1.9$, $\varphi_1 = 0.01$, $\varphi_2 = 0.1$ and $\alpha = 0.5$.

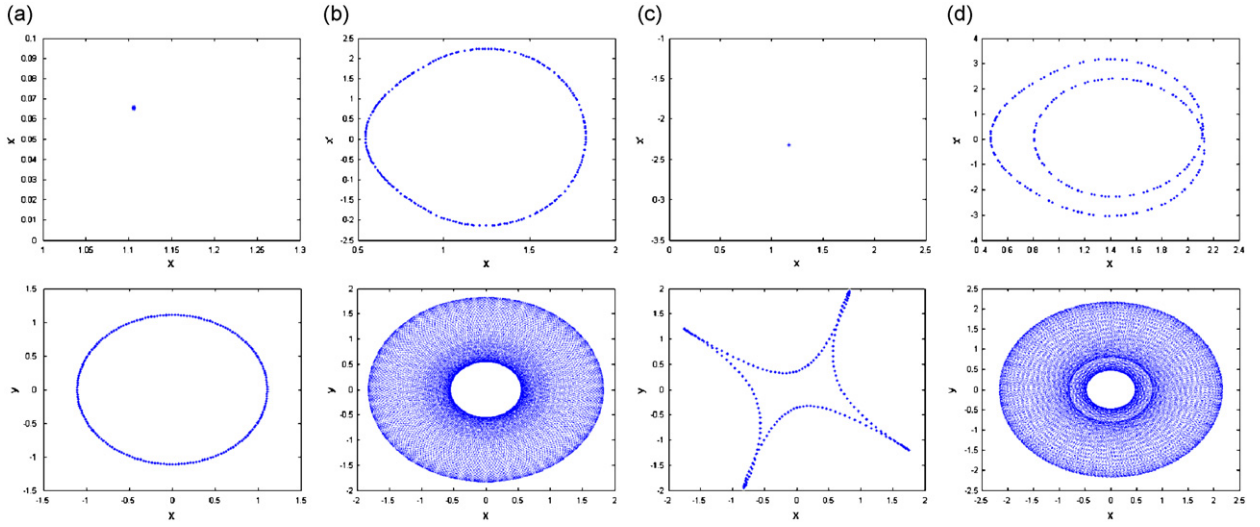

Fig. 7. The Poincaré maps and axes contrails of different Ω on the responses of the rubbing micro-rotor system with $\zeta = 0.025$ and $\rho = 0.5$: (a) $\Omega = 1.8$; (b) $\Omega = 3.0$; (c) $\Omega = 3.55$; and (d) $\Omega = 3.75$.

aspects. Therefore, it is valuable to investigate various dynamic characteristics of a rub-impact micro-rotor system for diagnosing the rotor-to-stator rub fault by using imbalance as the control parameter in MEMS.

Fig. 9 illustrate the bifurcation diagram of ρ on the response of rubbing micro-rotor system with $\zeta = 0.025$ and $\Omega = 4$ and $\zeta = 0.025$, $\Omega = 4$, $L_s/L_{|W|} = 1$, $L/L_{|W|} = 0.9$, $D = 1.9$, $\varphi_1 = 0.01$, $\varphi_2 = 0.1$ and $\alpha = 0.5$, respectively. It can be observed that system responses exhibit the alternation of periodic, quasi-periodic and chaotic motions at the interval of $0 < \rho < 1.2$. At $\rho < 0.18$, the system responses mainly display steady-state synchronous motion with P-1, the vibration amplitude of the micro-rotor is small and the rub phenomenon generally does not occur, as displayed in Fig. 9(a). As the imbalance increases, the vibration amplitude of the micro-rotor becomes bigger and the rub phenomenon occurs between the rotor and stator. When $\rho > 0.82$, the system response comes into chaotic motion and exhibits a wider range of chaotic motion as the control parameters vary. It is indicated that the changes of system responses are very complex as the imbalance varies and the motion displays alternation between periodic, quasi-periodic and chaotic motions. When the scale effects in friction are considered for a small ratio $L_s/L_{|W|} = 1$, scale length $L/L_{|W|} = 0.9$ and fractal dimension

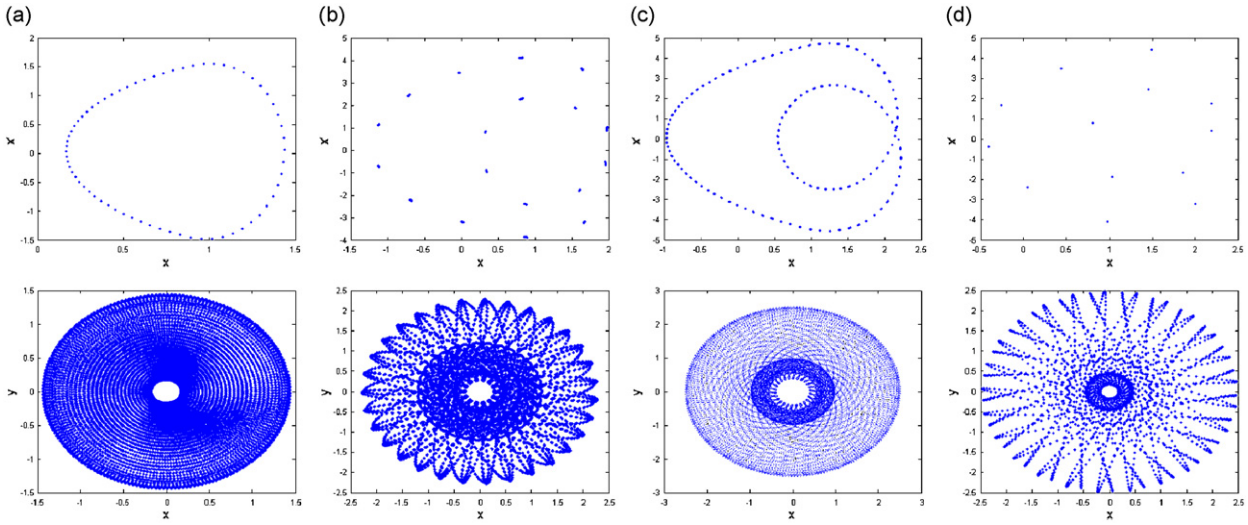

Fig. 8. The Poincaré maps and axes contrails of different Ω on the responses of the rubbing micro-rotor system with $\zeta = 0.025$, $\rho = 0.5$, $L_s/L_{|w|} = 1$, $L/L_{|w|} = 0.9$, $D = 1.9$, $\varphi_1 = 0.01$, $\varphi_2 = 0.1$ and $\alpha = 0.5$: (a) $\Omega = 1.8$; (b) $\Omega = 3.0$; (c) $\Omega = 3.55$; and (d) $\Omega = 3.75$.

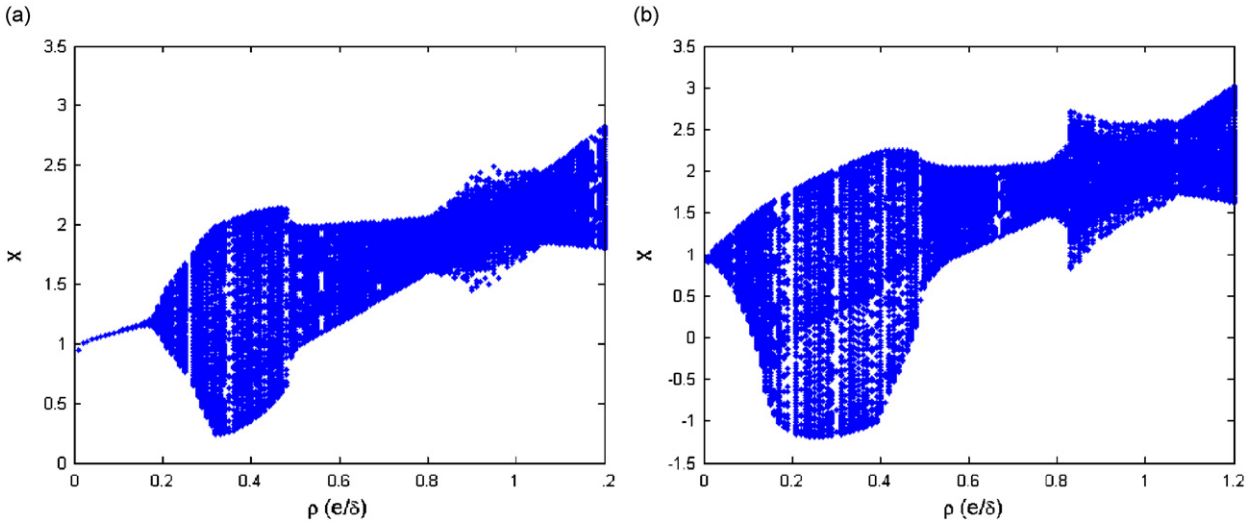

Fig. 9. The bifurcation diagram of ρ on the response of rubbing micro-rotor system: (a) $\zeta = 0.025$ and $\Omega = 4$; (b) $\zeta = 0.025$, $\Omega = 4$, $L_s/L_{|w|} = 1$, $L/L_{|w|} = 0.9$, $D = 1.9$, $\varphi_1 = 0.01$, $\varphi_2 = 0.1$ and $\alpha = 0.5$.

$D = 1.9$, the system response appears quasi-periodic motion from synchronous motion with P-1 at $\rho < 0.18$, the ranges of quasi-periodic and chaotic motions become wider, as shown in Fig. 9(b).

Fig. 10 illustrate the Poincaré maps, axes contrails, phase plane portraits and time histories on the responses of the rubbing micro-rotor system for different ρ. It can be seen that the system response comes into periodic motion from quasi-periodic motion, then leaves quasi-periodic motion and enters chaotic motion, and finally turns into quasi-periodic motion from chaotic motion. At $\rho = 0.12$, the Poincaré map has a closed curve and the axes contrails and phase plane portraits are regular and the corresponding Lyapunov exponent is zero. All of these prove that the motion is quasi-periodic. The system response change correspondingly with the increase of imbalance. At $\rho = 0.49$, the Poincaré map, axes contrails and phase plane portraits indicate that the motion of the micro-rotor system is periodic. At $\rho = 0.90$, the Poincaré map appears strange attractor and axes contrail and phase plane portrait show irregular distributions. All of these indicate that the response of the system enters chaotic motion from periodic motion. It can be observed from the Poincaré map

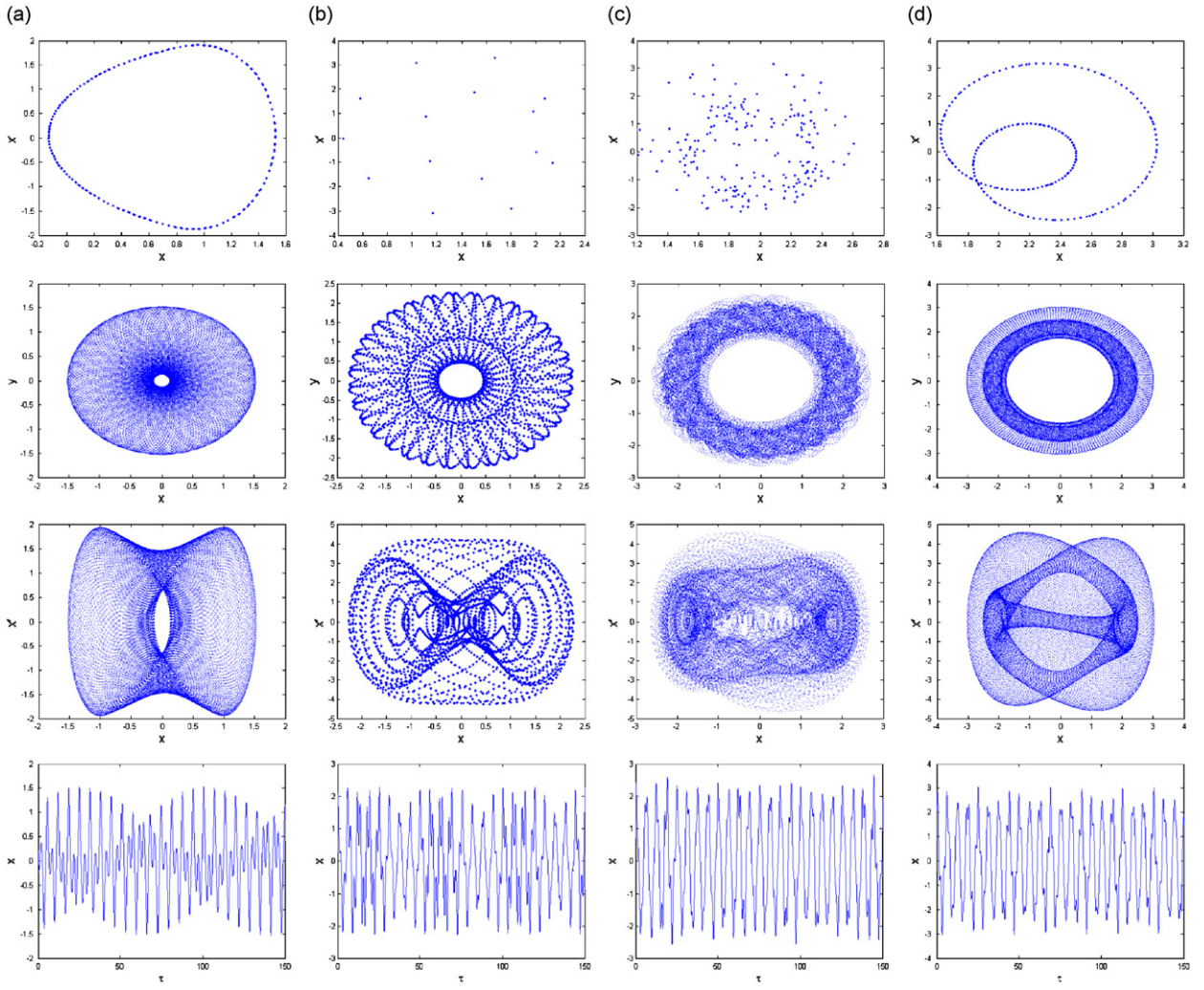

Fig. 10. The Poincaré maps, axes contrails, phase plane portraits and time histories of different ρ on the responses of the rubbing micro-rotor system with $\zeta = 0.025$, $\Omega = 4$, $L_s/L_{|w|} = 1$, $L/L_{|w|} = 0.9$, $D = 1.9$, $\varphi_1 = 0.01$, $\varphi_2 = 0.1$ and $\alpha = 0.5$: (a) $\rho = 0.12$; (b) $\rho = 0.49$; (c) $\rho = 0.90$; and (d) $\rho = 1.20$.

(see Fig. 10(a)–(d)) that the responses of the micro-rotor system alternate among the periodic, quasi-periodic and chaotic motions. At the same time, the time histories have corresponding changes.

4.1.3. *Effect of damping coefficient*

From the viewpoint of physics, the Jeffcott micro-rotor system is a dissipation system due to the existence of damping. For chaotic vibration it can be seen later that as the damping increases the amplitude of vibration becomes smaller. The system parameters for the computation are as follows: rotating speed $\Omega = 5$, scale parameters $\varphi_1 = 0.01$ and $\varphi_2 = 0.1$, impact factor $\alpha = 0.5$, integration step numbers $N = 200$and bifurcation step $\Delta\zeta = 0.005$.

Fig. 11 is the bifurcation diagram of ζ on the response of the rubbing micro-rotor system at the interval of $0.02 < \zeta < 0.06$ for different combinations of scale length parameters and fractal dimensions. The response of the micro-rotor system undergoes a complete process from quasi-periodic motion through chaotic and periodic motions to P-1 motion. In Fig. 11(a) and (b), as the fractal dimension D increases from 1.1 to 1.9, the components of quasi-periodic and chaotic motions decrease and the components of synchronous motion with P-1 increase at high damping coefficients. With the decrease of scale length $L/L_{|W|}$ from 0.9 to 0.6, the range

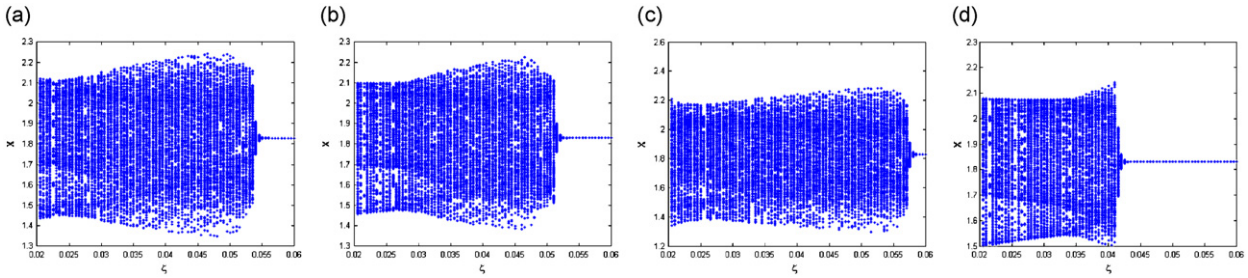

Fig. 11. The bifurcation diagram of ζ on the response of rubbing micro-rotor system with $\rho = 0.5$, $\Omega = 5$, $\varphi_1 = 0.01$, $\varphi_2 = 0.1$ and $\alpha = 0.5$: (a) $L_s/L_{|w|} = 1$, $L/L_{|w|} = 0.9$, $D = 1.1$; (b) $L_s/L_{|w|} = 1$, $L/L_{|w|} = 0.9$, $D = 1.9$; (c) $L_s/L_{|w|} = 1000$, $L/L_{|w|} = 0.6$, $D = 1.9$; and (d) $L_s/L_{|w|} = 1000$, $L/L_{|w|} = 0.9$, $D = 1.9$.

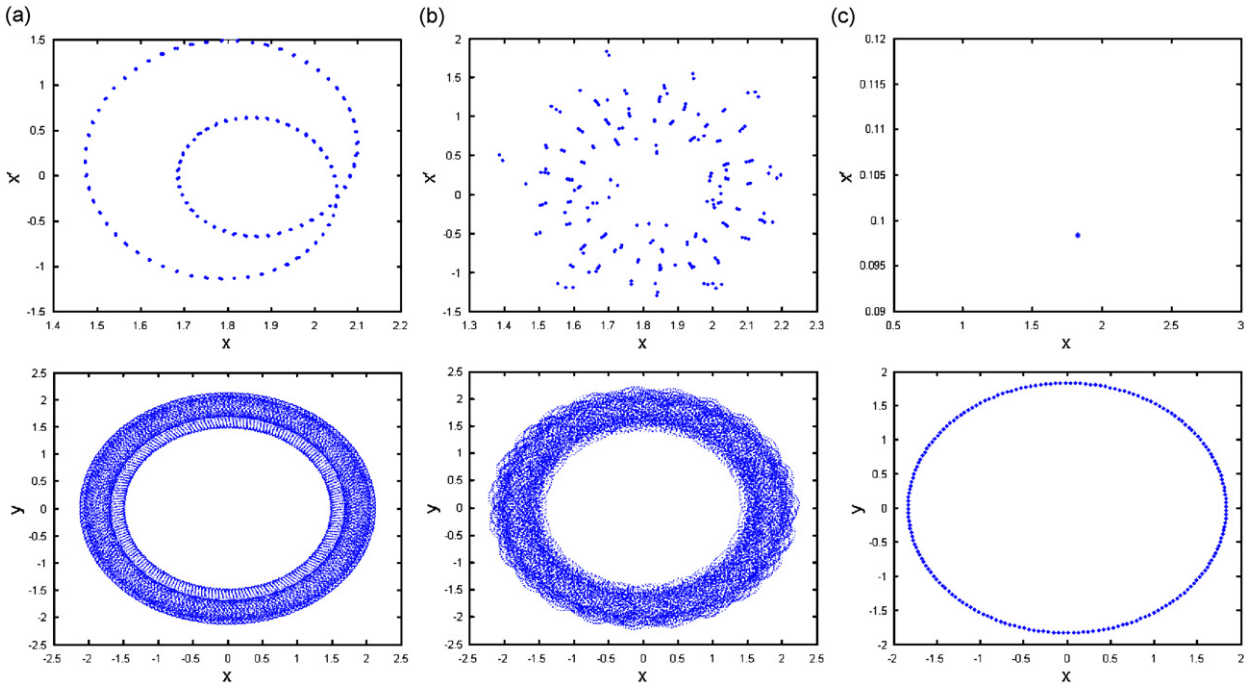

Fig. 12. The Poincaré maps and axes contrails of different ζ on the responses of the rubbing micro-rotor system with $\rho = 0.5$, $\zeta = 0.025$, $\Omega = 5$, $L_s/L_{|w|} = 1$, $L/L_{|w|} = 0.9$, $D = 1.9$, $\varphi_1 = 0.01$, $\varphi_2 = 0.1$ and $\alpha = 0.5$: (a) $\zeta = 0.025$; (b) $\zeta = 0.045$; and (c) $\zeta = 0.055$.

of quasi-periodic and chaotic motions become little wider, as shown in Fig. 11(b) and (c). When the scale ratio $L_s/L_{|W|}$ changes from 1 to 1000, the components of quasi-periodic and chaotic motions are replaced by periodic-one motions at high damping coefficients, as illustrated in Fig. 11(b) and (d).

The Poincaré maps and axes contrails for different damping coefficients are shown in Fig. 12. When the damping coefficient is small, i.e. $\zeta = 0.025$, the exhibited motion is quasi-periodic motion and its attractor is a closed curve. As the damping coefficient becomes larger, the closed form of the attractor is decomposed and the points in the Poincaré map gradually scatters. At $\zeta = 0.045$, the motion becomes a chaotic motion. After that the points of the attractor are decomposed again and finally converge to one point. When $\zeta = 0.055$, a synchronous motion with P-1 can be observed.

It can be seen that when the damping coefficient is used as the control parameter the motion changes from quasi-periodic motion through chaotic motion and periodic motion to synchronous motion with P-1. Therefore, the existence of damping has a certain effect on dynamic characteristics of the micro-rotor system. It is indicated that increasing damping can effectively suppress chaotic vibration.

4.1.4. Effect of fractal dimension

When a surface is magnified as an image looked very similar to the original surface, which is known as self-similarity in a fractal model [17,25]. The fractal model describes the surface profile as a self-similar structure, which is characterized by a fractal dimension and a scale coefficient. The fractal dimension is both scale invariant and is closely related to self-similarity.

To elucidate the physical significance of the fractal dimension on the surface topography in MEMS, the profiles of two rough surfaces are simulated and displayed in Fig. 13. From Eq. (8), a random surface profile cannot be simulated at $x = 0$ because the phases coincide at all frequencies. Thus, in the present analysis the portion of the simulated profile in the range $L_s < x < L$, where $L_s = 100\,\text{nm}$ and $L = 1100\,\text{nm}$, was used to model the real sample surface in x direction. Since γ determines the density of the spectrum, a choice of $\gamma = 1.5$ provides both the phase randomization and high spectral density. Fig. 13 shows that a smoother topography can be observed with a larger value of the fractal dimension D for fixed fractal roughness parameter G.

Fig. 14 is the bifurcation diagram of the micro-rotor system using the fractal dimension D as the control parameter with $\rho = 0.5$, $\zeta = 0.04$, $\Omega = 4$, $L/L_{|W|} = 0.6$, $\varphi_1 = 0.01$, $\varphi_2 = 0.1$, $\alpha = 0.5$, and bifurcation step $\Delta D = 0.01$ for different scale ratios. Fig. 14(a) shows the bifurcation diagram when the fractal dimension D is used as the control parameter at $L_s/L_{|W|} = 0$. A complete process from quasi-periodic motion to synchronous motion with P-1 can be seen at the interval of $1.1 < D < 1.9$. As the scale ratio becomes larger from $L_s/L_{|W|} = 0$ to $L_s/L_{|W|} = 1$, the bifurcation diagram is plotted in Fig. 14(b). It can be observed that the region of the synchronous motion with P-1 disappears while that of the quasi-periodic motion becomes wider as the scale ratio increases. Moreover, periodic motions appear at some fractal dimensions, such as the motion with period-nine (P-9) at $D = 1.39$.

Fig. 15 illustrates the Poincaré map, axes contrail, phase plane portrait and time history on the responses of the rubbing micro-rotor system for $D = 1.2$. It can be seen that the Poincaré map has a closed curve and the axes contrails and phase plane portraits are regular in system response and the corresponding Lyapunov exponent is zero. All of these prove that the motion is quasi-periodic.

4.1.5. Effect of scale length

The change of scale length affects the coefficient of friction and result in the responses of the rubbing micro-rotor system being varied. Fig. 16 is the bifurcation diagram of $L/L_{|W|}$ on the response of the rubbing micro-rotor system at the interval of $0.1 < L/L_{|W|} < 1$ for various combinations of $L_s/L_{|W|}$ and D. It can be observed that the response of the micro-rotor system has a complete process from quasi-periodic motion through

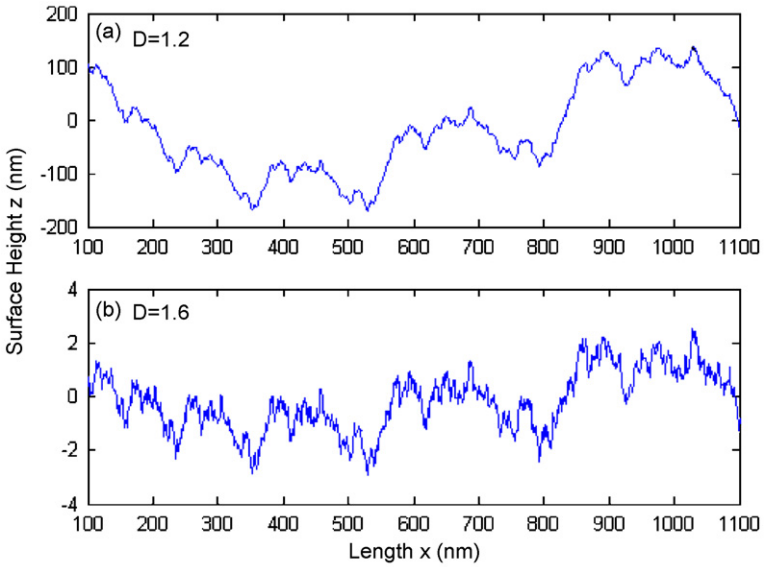

Fig. 13. Simulation of two-dimensional fractal surface profiles with $G = 1 \times 10^{-11}\,\text{m}$: (a) $D = 1.2$; and (b) $D = 1.6$.

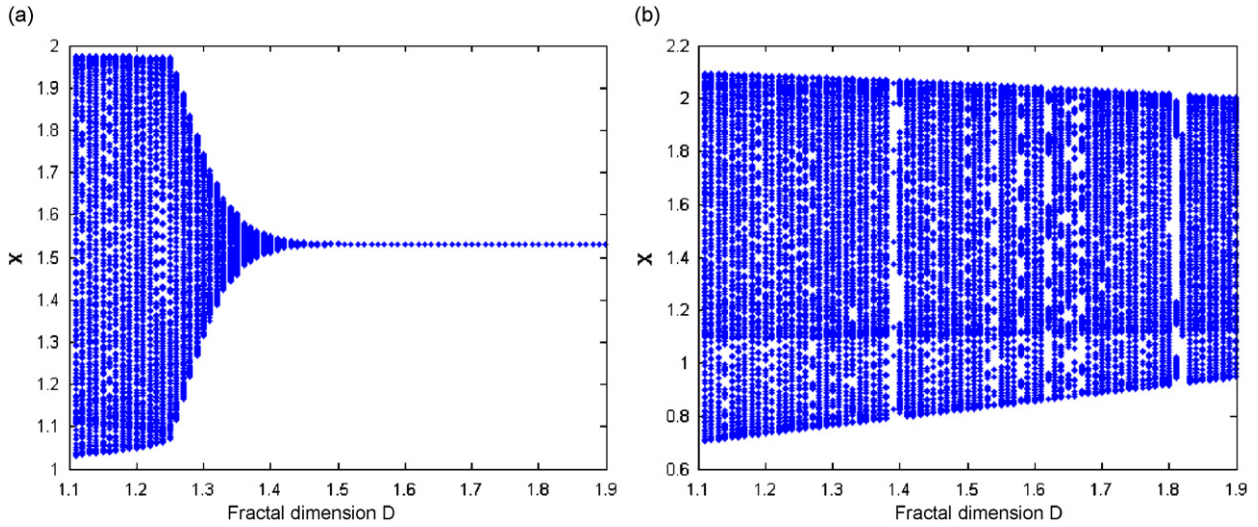

Fig. 14. The bifurcation diagram of D on the response of rubbing micro-rotor system with $\rho = 0.5$, $\zeta = 0.04$, $\Omega = 4$, $L/L_{|w|} = 0.6$, $\varphi_1 = 0.01$, $\varphi_2 = 0.1$ and $\alpha = 0.5$: (a) $L_s/L_{|w|} = 0$; and (b) $L_s/L_{|w|} = 1$.

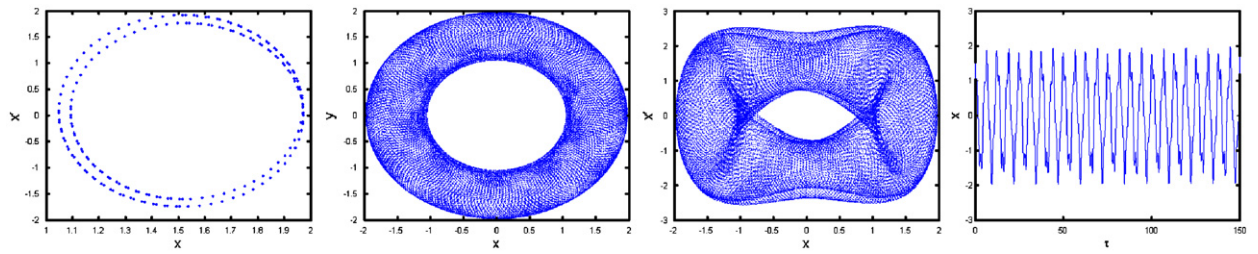

Fig. 15. The Poincaré map, axes contrail, phase plane portrait and time history on the responses of the rubbing micro-rotor system with $D = 1.2$ and $L_s/L_{|w|} = 0$.

periodic motions to P-1 or quasi-periodic motion. As the fractal dimension D increases from 1.1 to 1.6, the components of quasi-periodic motion decrease and the components of synchronous motion with P-1 increase at high fractal dimension, as shown in Fig. 16(a) and (b). In Fig. 16(c), with the increase of scale ratio $L_s/L_{|W|}$ from 0 to 1, the range of quasi-periodic motion becomes wider and the motion with P-1 disappears. When the scale ratio $L_s/L_{|W|}$ decreases from 1 to 0.1 and the fractal dimension D increases from 1.6 to 1.9 simultaneously, the components of quasi-periodic and periodic motions are changed alternately and the ranges of them become wider, as illustrated in Fig. 16(d). It is indicated that the possibility of rub becomes more and more obvious as the increase of the friction coefficient at lower scale length.

4.2. Discussions

Advances of MEMS technology make understanding of scale effects in friction especially important and microscale and nanoscale measurements demonstrate the scale dependence of friction as well as mechanical properties [17–19]. Bhushan and Kulkarni [27] used an atomic force microscope (AFM) to measure the friction of a Si_3N_4 tip compared to those for Si, SiO_2, and natural diamond and obtained that the coefficient of friction depends on the applied load and scale effects. Bhushan et al. [17–19,27] reported that the coefficient of friction measured for Si(1 0 0) DLC, Z-DOL, and HDT at microscale in dry and wet environments are scale dependent. In the case of elastic contact, the coefficient of friction decreases with decreasing scale, while it may increase or decrease with scale for the case of plastic contact. It is noted that the critical value of loads for Si

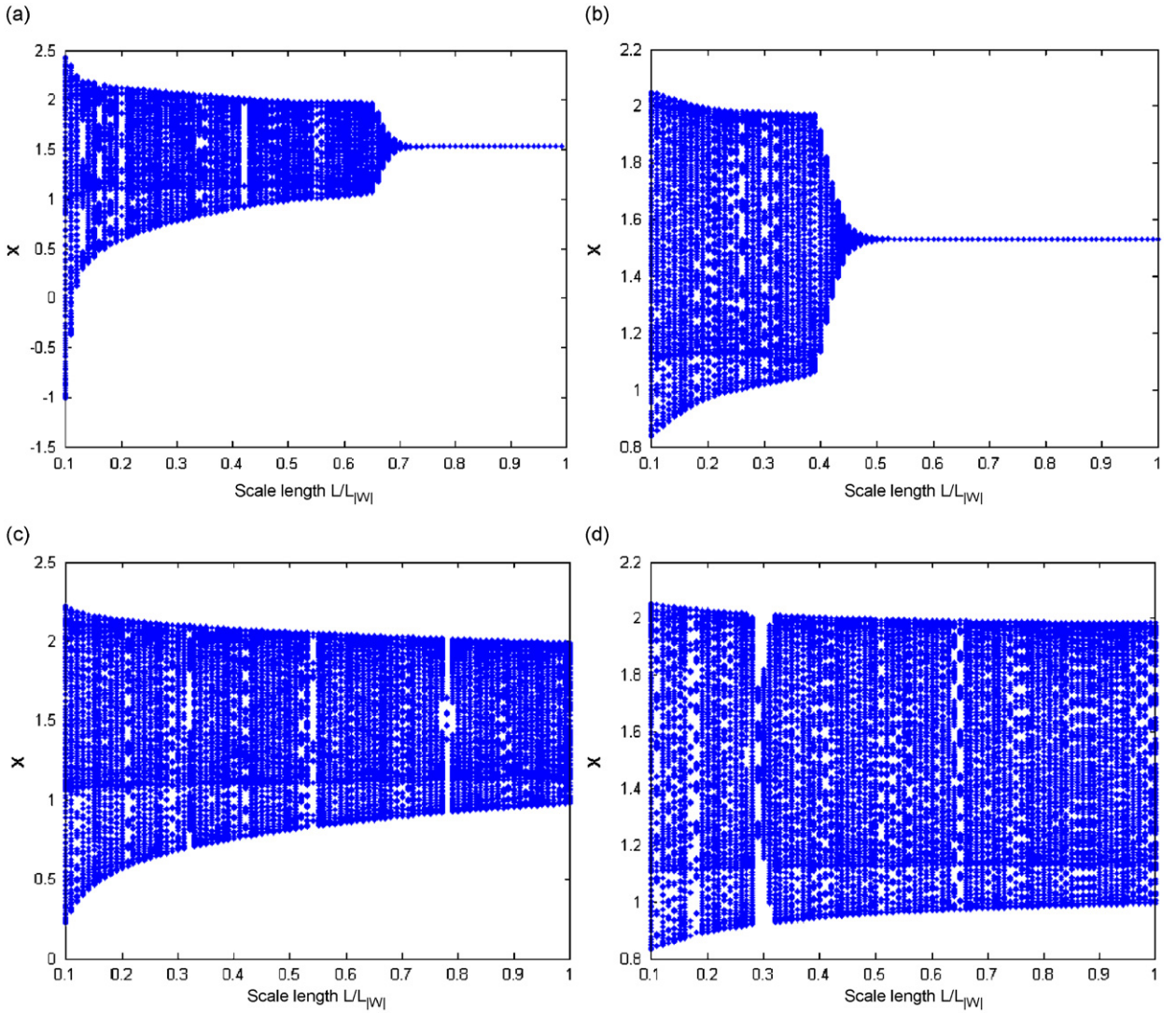

Fig. 16. The bifurcation diagram of $L/L_{|w|}$ on the response of rubbing micro-rotor system with $\rho = 0.5$, $\zeta = 0.04$, $\Omega = 4$, $\phi_1 = 0.01$, $\phi_2 = 0.1$ and $\alpha = 0.5$: (a) $L_s/L_{|w|} = 0$, $D = 1.1$; (b) $L_s/L_{|w|} = 0$, $D = 1.6$; (c) $L_s/L_{|w|} = 1$, $D = 1.6$; and (d) $L_s/L_{|w|} = 1$, $D = 1.9$.

and SiO_2 corresponds to stresses equal to their hardness values, which suggests that the transition to plasticity plays a role in this effect [18]. During transition from elastic to plastic regime, three components of the coefficient friction in Eq. (7) will change. In the elastic regime, the dominant contribution is expected to be adhesion involving elastic deformation, and in the plastic regime the dominant contribution is expected to be deformation [19]. Moreover, deformation component of friction can be reduced by reducing surface roughness, selecting materials of more or less equal hardness and removing wear and contaminant particles from the interface [23]. Therefore, further modeling should be considered to study the transition effect and the scale effects in friction should be taken into account for investigating the dynamic characteristics of micro-rotating machinery in MEMS.

When two bodies come into contact, the contact occurs only on high asperities or summits, and the real area of contact is a small fraction the apparent area of contact. Multiple asperities of two rough surfaces in contact have irregular shapes and two of them, including conical and spherical shapes, have been studied comparatively. The scale dependence for the two-body deformation component of the coefficient of friction in

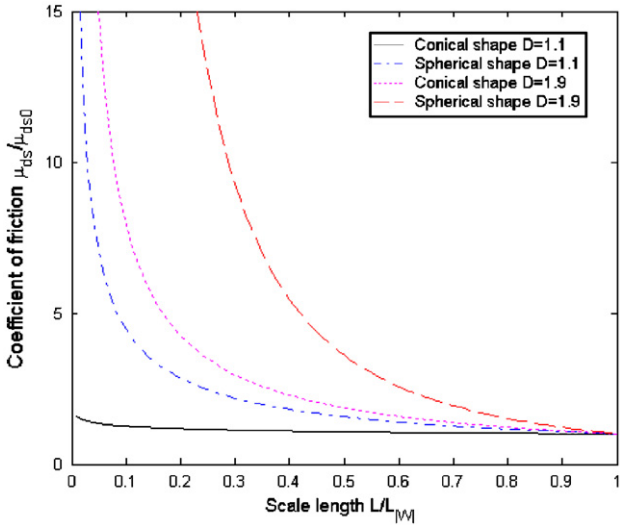

Fig. 17. Normalized component of the coefficient of dry friction due to two-body deformation for the fractal roughness with fractal dimension $D = 1.1$ and 1.9.

Eq. (4) is displayed in Fig. 17 for conical and spherical shape asperities with two values of the fractal dimension $D = 1.1$ and 1.9. It is observed that the coefficients of friction increase with decreasing scale and they are larger for spherical shape asperity than those for conical shape asperity.

In our previous work [22] and above several sections, the radial stiffness of the stator is supposed to be linear and the radial rub-impact force between the rotor and stator is assumed to be in direct proportion to the radial displacement at the contact point. To a certain extent, the results give a qualitative explanation of some rotor rubbing phenomena, but cannot explain the rich high frequency components and non-periodical motions existed in rotor responses. Results from the investigations on elastic contact issues in micro-rotating machinery indicate that the relationship between the force and displacement of two relative sliding bodies in contact is nonlinear and it relates with the shape of contact surfaces and material parameters of contact bodies [11–14]. The surfaces of the rotor and stator are rough and have large numbers of asperities. Since the heights of the asperities are different and the distributions of them are stochastic, the contact points between the stator and rotor under the applied loads. At the beginning, only a few asperities come into contact, then the number of contact asperities increases with the increase of applied load. The previous contact asperities come into elastic deformation on high summits with the increase of applied load, and the plastic deformation will take place when the contact stress is beyond the stress yield. Therefore, the asperities at the interface of the rotor and stator take place deformation, either elastic deformation or plastic deformation. The relationship between the stress and strain of elastic deformation is linear, but that of plastic deformation is nonlinear. Considering these characteristics, the relationship between the normal contact force and displace of the stator and rotor can be supposed by

$$F_N = k_r(u - \delta)^{q/r}, \tag{26}$$

where q, r can be chosen as 1, 2, 3, … in terms of contact forms.

Fig. 18 displays the bifurcation diagram of the micro-rotor system using the rotating speed as the control parameter with $\rho = 0.5$, $\zeta = 0.04$, $L_s/L_{|W|} = 1$, $L/L_{|W|} = 0.9$, $D = 1.9$, $\varphi_1 = 0.01$, $\varphi_2 = 0.1$, $\alpha = 0.5$, $q = 2$ and $r = 1$. It can be seen that the rotor responses contains synchronous motion with P-1 and quasi-periodic motion at the interval of $0 < \Omega < 5$. When $\Omega < 3.45$, the vibration amplitude of the micro-rotor is smaller, the rub phenomenon does not occur, the motion is synchronous motion with P-1, and only one point is correspondingly shown in the bifurcation diagram for every rotating speed. With the increase of the rotating speed, rub does occur between the rotor and the stator. As $\Omega > 3.45$, the motion becomes quasi-periodic. Moreover, with the increase of damping coefficient and the addition of plastic contact term, the components

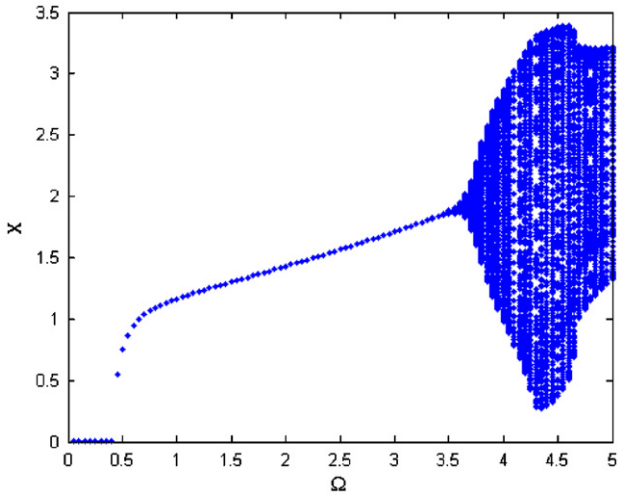

Fig. 18. The bifurcation diagram of Ω on the response of rubbing micro-rotor system with $\rho = 0.5$, $\zeta = 0.04$, $L_s/L_{|w|} = 1$, $L/L_{|w|} = 0.9$, $D = 1.9$, $\varphi_1 = 0.01$, $\varphi_2 = 0.1$, $\alpha = 0.5$, $q = 2$ and $r = 1$.

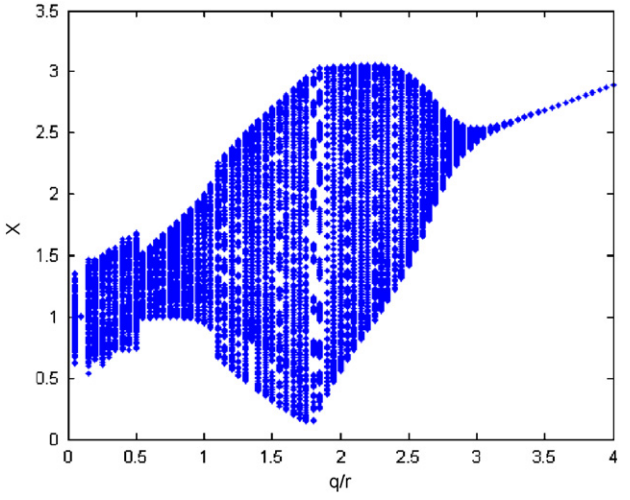

Fig. 19. The bifurcation diagram of q/r on the response of rubbing micro-rotor system with $\rho = 0.5$, $\zeta = 0.04$, $\Omega = 4$, $L_s/L_{|w|} = 1$, $L/L_{|w|} = 0.9$, $D = 1.9$, $\varphi_1 = 0.01$, $\varphi_2 = 0.1$ and $\alpha = 0.5$.

of synchronous motions with P-1 increase and the quasi-periodic motions become wider compared with Fig. 6. Therefore, as the rotating speed increases, the changes of the system responses are very complex and mainly include periodic and quasi-periodic motions alternately.

Fig. 19 shows the bifurcation diagram of q/r on the response of rubbing micro-rotor system with $\rho = 0.5$, $\zeta = 0.04$, $\Omega = 4$, $L_s/L_{|W|} = 1$, $L/L_{|W|} = 0.9$, $D = 1.9$, $\varphi_1 = 0.01$, $\varphi_2 = 0.1$ and $\alpha = 0.5$. It can be observed that the system response comes into chaotic motion from quasi-periodic motion, then leaves chaotic motion and enters quasi-periodic motion, and finally turns into P-1 motion. The Poincaré maps and axes contrails are displayed in Fig. 20 for different q/r. When $q/r = 0.15$, the Poincaré map appears strange attractor and the axes contrail has irregular distributions. All of these figures show that the system response enters into chaotic motion from periodic motion. At $q/r = 1$ and $q/r = 2$, the Poincaré maps have closed curves and the axes contrails are regular, the exhibited motions are quasi-periodic. As the value of q/r increases, a synchronous motion with P-1 can be seen at $q/r = 4$. The results indicate that the components of system responses show

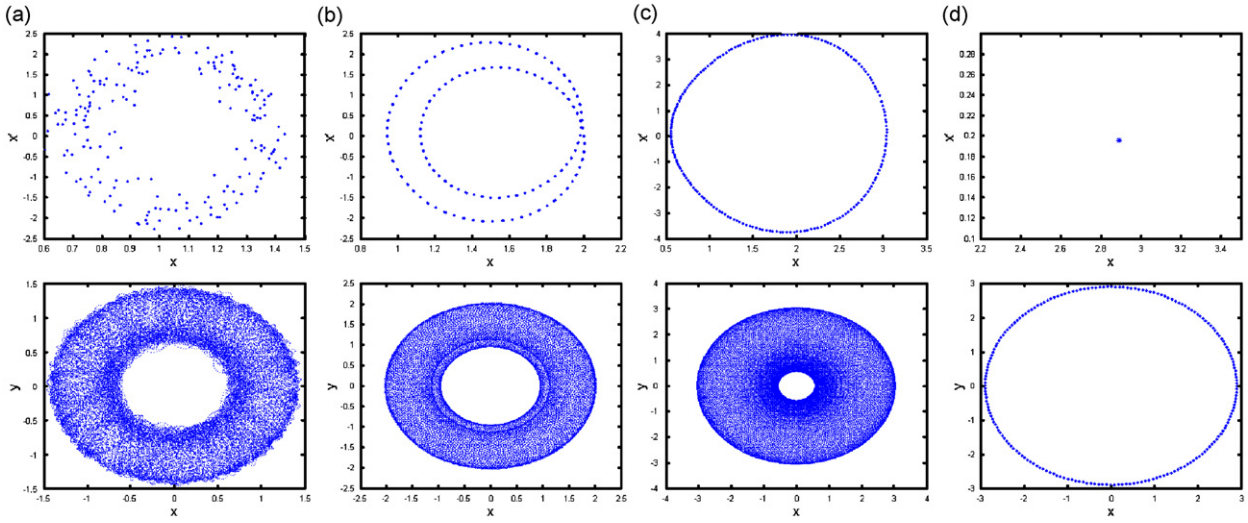

Fig. 20. The Poincaré maps and axes contrails of various q/r on the responses of the rubbing micro-rotor system with $\rho = 0.5$, $\zeta = 0.04$, $\Omega = 4$, $L_s/L_{|w|} = 1$, $L/L_{|w|} = 0.9$, $D = 1.9$, $\varphi_1 = 0.01$, $\varphi_2 = 0.1$ and $\alpha = 0.5$: (a) $q/r = 0.15$; (b) $q/r = 1$; (c) $q/r = 2$; and (d) $q/r = 4$.

quasi-periodic and chaotic motions for $q/r < 1$, while they display quasi-periodic motions and synchronous motions with P-1 for $q/r > 1$.

5. Conclusions

Since there is a large surface-to-volume ratio, friction force becomes serious tribological concerns that limit the life and reliability of MEMS devices. The stability of the rub solutions of a nonlinear Jeffcott micro-rotor system are analyzed. The results make it possible to get the boundaries of different micro-rotor response characteristics in the parameter space. The effects of the system parameter combinations on the dynamic behaviors are investigated according to the analytical stability conditions. The stable boundaries vary correspondingly to the change of system parameters, and the rub motion will occur less with the decrease of the imbalance or friction coefficient. The increase of damping can control the occurrence of the rub motion. It is observed that the unstable rub motion will occur less with the decrease of imbalance.

Nonlinear characteristics of a rub-impact micro-rotor system with the scale effects in friction in MEMS have been investigated to unveil the global dynamic behavior. Both the qualitative theoretical analysis and quantitative numerical simulation demonstrate that the nonlinear rub-impact caused by the rotating speed, rotor imbalance, damping coefficient, scale length, fractal dimension and nonlinear rub-impact force makes the dynamic characteristics of the micro-rotor system alternate among stable periodic, quasi-periodic and chaotic states. It is clear that micro-tribology is an important factor affecting the performance and reliability of micro-rotating machinery in MEMS. There is a need to develop a fundamental understanding of contact, friction, wear phenomena on the scale pertinent to MEMS/NEMS and to understand the role of surface contamination and environment in micro-rotating machinery. Furthermore, it is necessary to develop lubricants and identify lubrication methods that are suitable for MEMS-based rotating machinery. Future work should include the development of models of rough surface topography and the effects of distributions of asperity heights and shapes, asperity coupling, scale-dependent plasticity, transition from the elastic to plastic regime, interface temperature and experiments to validate the models.

Acknowledgements

The authors are grateful to Dr. K.X. Wei and H. Huang for their fruitful suggestions and discussions. This work was supported by the National Natural Science Foundation of China under Grant nos. 10602033 and

50575132, the National Outstanding Youth Foundation of China under Grant no. 10325209, and the China Postdoctoral Science Foundation under Grant no. 20060400165.

References

[1] W.S. Trimmer, K.J. Gabriel, Design considerations for a practical electrostatic micromotor, *Sensors and Actuators A* 11 (1987) 189–206.
[2] A.H. Epstein, S.D. Senturia, G. Anathasuresh, A. Ayon, K. Breure, K.-S. Chen, F.E. Ehrich, G. Gauba, R. Ghodssi, C. Groshcnry, S. Jacobson, J.H. Lang, C.-C. Lin, A. Mchra, J.M. Miranda, S. Nagle, D.J. Orr, E. Piekos, M.A. Schrnidt, G. Shirley, M.S. Spearing, C.S. Tan, Y.-S. Tzang, I.A. Waitz, Power MEMS and microengines, *Proceedings of the 1997 International Conference on Solid-State Sensors and Actuators*, Chicago, IL, June 16–19, 1997, pp. 753–756.
[3] E. Piekos, K.S. Breuer, Pseudo-spectral orbit simulation of non-ideal gas-lubricated journal bearings for microfabricated turbomachines, *Journal of Tribology* 121 (1999) 604–609.
[4] L.G. Frechette, S.A. Jacobson, K.S. Breuer, F.F. Ehrich, et al., High-speed microfabricated silicon turbomachinery and fluid film bearings, *Journal of Microelectromechanical Systems* 14 (1) (2005) 141–152.
[5] N. Miki, C.J. Teo, L.C. Ho, X. Zhang, Enhancement of rotordynamic performance of high-speed micro-rotors for power MEMS applications by precision deep reactive ion etching, *Sensors and Actuators A* 104 (2003) 263–267.
[6] S.F. Bart, M. Mehregany, L.S. Tavrow, J.H. Lang, S.D. Senturia, Electric micromotor dynamics, *IEEE Transactions on Electron Devices* 39 (3) (1992) 566–575.
[7] A.H. Epstein, Millimeter-scale, MEMS gas turbine engines, *Proceedings of the ASME Turbo Expo 2003 Power for Land, Sea, and Air Altanta*, Georgia, USA, June 2003, pp. 1–28.
[8] A. Endemano, J.Y. Fourniols, H. Camon, A. Marchese, VHDL-AMS modelling and simulation of a planar electrostatic micromotor, *Journal of Micromechanics and Microengineering* 13 (2003) 580–590.
[9] Y.C. Tai, R.S. Muller, Frictional study of IC-processed micromotor, *Sensors and Actuators* 21 (1990) 180–183.
[10] U. Beerschwinger, N.G. Milne, S.J. Yang, R.L. Reuben, A.J. Sangster, H. Ziad, Coupled electrostatic and mechanical FEA of a micromotor, *Journal of Microelectromechanical Systems* 3 (1994) 162–171.
[11] W.M. Zhang, G. Meng, Contact dynamics between the rotor and bearing hub in an electrostatic micromotor, *Microsystem Technologies* 11 (2005) 438–443.
[12] W.M. Zhang, G. Meng, Numerical simulation of sliding wear between the rotor bushing and ground plane in micromotors, *Sensors and Actuators A* 126 (2006) 15–24.
[13] W.M. Zhang, G. Meng, Friction and wear study of the hemispherical rotor bushing in a variable capacitance micromotor, *Microsystem Technologies* 12 (4) (2006) 283–292.
[14] W.M. Zhang, G. Meng, H.G. Li, Electrostatic micromotor and its reliability, *Microelectronics Reliability* 45 (2005) 1230–1242.
[15] J. Hurtado, K.-S. Kim, Scale effect in friction of single-asperity contacts. II. Multiple-dislocation-cooperated slip, *Proceedings of the Royal Society of London A* 455 (1999) 3385–3400.
[16] G.G. Adams, S. Muftu, M.M. Azhar, A scale-dependent model for multi-asperity contact and friction, *Journal of Tribology* 125 (2003) 700–708.
[17] B. Bhushan, M. Nosonovsky, Scale effects in dry and wet friction, wear, and interface temperature, *Nanotechnology* 15 (2004) 749–761.
[18] B. Bhushan, M. Nosonovsky, Scale effects in friction using strain gradient plasticity and dislocation-assisted sliding (microslip), *Acta Materialia* 51 (2003) 4331–4345.
[19] B. Bhushan, M. Nosonovsky, Comprehensive model for scale effects in friction due to adhesion and two- and three-body deformation (plowing), *Acta Materialia* 52 (2004) 2461–2474.
[20] G.G. Adams, S. Muftu, Improvements to a scale-dependent model for contact and friction, *Journal of Physics D: Applied Physics* 38 (2005) 1402–1409.
[21] N. Tambe, B. Bhushan, Friction model for the velocity dependence of nanoscale friction, *Nanotechnology* 16 (2005) 2309–2324.
[22] W.M. Zhang, G. Meng, Stability, bifurcation and chaos of a high-speed rub-impact rotor system in MEMS, *Sensors and Actuators A* 127 (1) (2006) 163–178.
[23] B. Bhushan, *Introduction to Tribology*, Wiley, New York, 2002, pp. 214–231.
[24] N. Yu, A.A. Polycarpou, Combining and contacting of two rough surfaces with asymmetric distribution of asperity heights, *Journal of Tribology* 126 (2004) 225–232.
[25] A. Majumdar, B. Bhushan, Role of fractal geometry in roughness characterization and contact mechanics of surfaces, *Journal of Tribology* 112 (1990) 205–216.
[26] E.J. Berger, Friction modeling for dynamic system simulation, *Applied Mechanical Reviews* 55 (6) (2002) 535–577.
[27] B. Bhushan, A.V. Kulkarni, Effect of normal load on microscale friction measurements, *Thin Solid Films* 278 (1996) 49–56.